JNP Journal of Nanophotonics

RESEARCH PAPER

Fabrication of silver-decorated zinc oxide nanowire sensor in microchannels for surface-enhanced Raman spectroscopy

Andrew L. Cook and Todd D. Giorgio*
Vanderbilt University, Department of Biomedical Engineering, Nashville, Tennessee, United States

ABSTRACT. Surface-enhanced Raman spectroscopy (SERS) performed in microfluidic channels offers multiple benefits to the sensitive and reliable detection of dilute analytes while utilizing the advantages of microfluidics, including small samples, high throughput, and portability. Physical deposition of metallic nanoparticles by techniques, such as electron beam deposition, results in dense populations of nanoparticles and hot-spots between nanoparticles for sensitive detection. However, not only do physically deposited SERS-active surfaces necessitate additional steps during device fabrication, but also surface fabrication is itself complicated by the constraints imposed by the microfluidic channel. Our work demonstrates a robust approach to the physical fabrication of an SERS-active substrates inside a poly(dimethylsiloxane) (PDMS) microfluidic channel. Direct growth of zinc oxide nanowires inside the PDMS channel and e-beam deposition of silver to coat the nanowires was performed before bonding PDMS to glass. This process enables label-free SERS sensing of micromolar crystal violet and melamine with minimal spectral interference from the PDMS-based channel.

Keywords: surface-enhanced Raman spectroscopy; ZnO nanowires; advanced growth and deposition; poly(dimethylsiloxane); microfluidics

Paper 24003G received Jan. 26, 2024; revised Jun. 17, 2024; accepted Jun. 24, 2024; published Jul. 17, 2024.

1 Introduction

Surface-enhanced Raman spectroscopy (SERS) that is integrated with microfluidic technology offers the advantages of reduced sample consumption and reaction time, high detection efficiency, and portability compared with other state-of-the-art detection paradigms.[1] This integration is primarily pursued through either colloidal solutions[2,3] or stationary substrates.[4–6] Co-injection of SERS-active colloids with samples into microfluidic channels can provide efficient sensing and heat dissipation, although this technique often suffers from aggregation, resulting in reduced reproducibility and poor mixing due to predominantly laminar flow in microfluidic channels.[7] Stationary substrates offer greater stability and reproducibility, although they are often less efficient than colloidal strategies because stationary substrates cannot be dispersed within sample fluids.[8,9]

SERS-active substrates based on nanowires decorated with metal nanoparticles, such as silver (Ag) or gold (Au), can minimize the drawbacks associated with colloidal or stationary substrate sensing when fabricated within a microfluidic channel. This design offers the stability and reproducibility similar to stationary substrates but can also provide the sensing efficiency of colloidal strategies due to their inherent three-dimensional architecture.[10,11] Metal-decorated zinc oxide

*Address all correspondence to Todd D. Giorgio, todd.d.giorgio@vanderbilt.edu

(ZnO) nanowires are an attractive platform for SERS sensing. ZnO is a biocompatible[12] wide direct-bandgap semiconductor with a band-edge emission of ~3.4 eV[13] and a high exciton binding energy of 60 meV.[14,15] These properties make ZnO nanowires electronically stable at room temperature[15] and transparent to visible and near-infrared (NIR) light,[16] reducing absorption of Raman scattered photons. Optical transparency is ideal for Raman spectra acquired through the substrate as is necessitated by the sensor and detector geometry that we anticipate in microfluidic technology. In addition, ZnO has been demonstrated to increase surface enhancement due to the charge transfer between ZnO and both Ag[17] and analytes directly adsorbed to the nanowires.[18] Additionally, crystalline ZnO possesses high electron mobility[19] and a large refractive index of ~2.0 in the visible region.[20,21] Combining these characteristics with the atomically smooth and highly faceted hexagonal single-crystal structure of ZnO nanowires can induce Mie scattering resonances. Mie scattering can reduce signal loss to scattering through waveguiding light[22] and synergize with the charge transfer to enhance Raman scattering up to 10^5, in addition to the electromagnetic mechanism of SERS.[23]

Microchannels can be fabricated from a variety of materials including thermoplastics such as polycarbonate or polymethylmethacrylate, silicon, or glass using techniques such as electron beam lithography, injection molding, hot embossing, or 3D printing, but soft-lithography using poly(dimethylsiloxane) (PDMS) has become the standard of microfluidic fabrication.[24] This is due to advantages such as useful feature resolution, low cost, and ease of fabrication.[25,26] Additionally, increased attention has been given in recent years to the development of flexible, transparent SERS substrates for applications including flexible electronics and photonics or conformal attachment to surfaces of interest.[27] Both the prevalence of PDMS-based microfluidics and the usefulness of flexible SERS substrates exemplify the benefit of fabricating SERS-active substrates directly onto PDMS.

During the fabrication of SERS-active microchannels, stationary substrates, such as the Ag-decorated ZnO nanowires, are usually fabricated on the glass wall of the channel. This is done to avoid spectroscopic interference by polymers commonly used to fabricate microfluidic channels, such as PDMS, which has its own strong Raman spectrum. ZnO nanowire fabrication on glass lends itself to *in situ* fabrication techniques, such as hydrothermal growth and electroplating after microchannel fabrication. In particular, metal-decorated ZnO nanowires can be fabricated *in situ* hydrothermally;[10,28,29] however, hydrothermal fabrication typically results in sparse metal nanoparticle formation.[10] By contrast, electron beam (e-beam) deposition as a physical technique forms denser nanoparticle distributions,[11,22] resulting in higher surface enhancement due to proximity-induced hotspots between nanoparticles.[30] However, one major drawback is that physical deposition of nanoparticles necessitates *ex situ* SERS substrate fabrication on glass prior to microfluidic channel bonding because closing the channel prevents the deposition of material from an external source. Alignment of the SERS sensor on glass with a microchannel in PDMS is complicated by microscale dimensions and the deformability of PDMS. The complexity of the accurate placement in PDMS microchannels is amplified for designs that include multiple SERS sensors on a single-glass substrate. Additional alignment steps limit the flexibility of microchannel design,[7] making it less ideal for the production of large numbers of disposable sensors. Fabricating SERS substrates directly into PDMS microchannels before bonding with glass, as illustrated by Fig. 1, enables the fabrication of complex multisensory, multichannel devices in the absence of rigorous alignment requirements.

In this study, we demonstrated that a ZnO nanowire substrate decorated with e-beam deposited Ag nanoparticles can be simply fabricated within a PDMS microchannel *ex situ* without requiring an alignment step to complete microchannel fabrication. Furthermore, we demonstrate that trace chemical and biological analytes can be detected through a PDMS microchannel wall by careful optimization of the device design and analysis of SERS optical signals.

2 Methods

To simplify the fabrication of an SERS-integrated microfluidic channel, Ag-decorated ZnO (Ag/ZnO) nanowires were fabricated directly into the channel such that the nanowires would reside on the "roof" of the channel after bonding with glass, as illustrated by Fig. 1. In this orientation, Raman spectra would be acquired through the "roof" of the channel. The first step in accomplishing this is to examine the effect of PDMS thickness on spectral intensity as

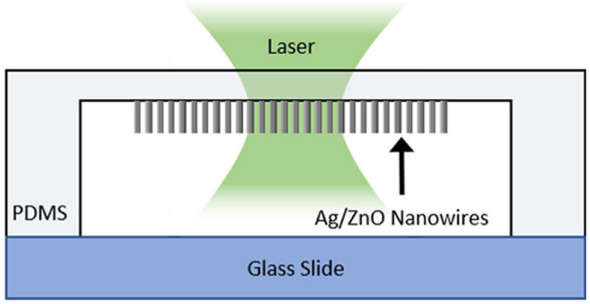

Fig. 1 Illustration of the cross section of a microchannel integrated with an Ag/ZnO nanoprobe fabricated on the PDMS.

crosslinked PDMS polymer is known to scatter light,[31] and Mao et al.[32] demonstrated 4× reduced SERS sensitivity when acquiring spectra through a PDMS cap. Furthermore, Meng et al.[33] offered evidence that surface plasmon resonance (SPR) sensor performance decreases when carried out through materials with high indices of refraction and that SPR performance is also dependent on the thickness of such materials. Next, the applicability of SERS through PDMS must be exemplified through SERS of a relevant analyte. Melamine is an industrial material primarily used in polymer manufacturing that has also been added to dairy products to produce artificially high readings of protein content. Because melamine can cause kidney failure and death, the Codex Alimentarius set a limit of 1 mg/L (7.93 μM) of melamine in powdered infant formula.[34] Using information gained from the previous two experiments, a PDMS channel must be designed and fabricated. The Ag/ZnO nanowire substrate needed to be constructed within the channel, so SERS of the analytes injected into the channel can be acquired.

2.1 ZnO Seed in PDMS Channel

SERS-active nanostructures were fabricated directly into the channel, such that they would reside on the "roof" of the channel, as shown in Fig. 1. Substrates and microchannels were fabricated from PDMS via soft lithography with Sylgard 184® (Dow Corning, Batch #H047ICL055), which consists of a liquid PDMS base and a curing agent. A microchannel master was designed in AutoCAD® 2017 as a mold for PDMS microchannels and machined from aluminum, as shown in Fig. 8. The base and curing agent were mixed at a 10:1 ratio and poured over the base. The solution was then placed in a vacuum chamber at ~25 mm Hg until all bubbles were removed. The lid was fitted onto the base before the dish was placed in the oven at 95°C for 2 h to cure the PDMS, after which the dishes were removed and allowed to cool at room temperature. After cooling, the master was cut away from the surrounding PDMS, and the microchannels were extracted.

PDMS microchannels were cleaned with the ALD-AMD method,[11] which consists of submersion in a 1% Alconox® solution, deionized (DI) water, acetone, methanol, and DI water, sequentially. At each step, the substrates were sonicated for 10 min. After this cleaning process was completed, the substrates were dried using nitrogen gas. For each microchannel, Kapton tape was used to mask the PDMS surface containing the channel, so only the channel was exposed. Microchannels were then mounted in a sputter deposition system (Angstrom Amod Multimode Deposition Chamber), which was pumped down to 5.5×10^{-6} Torr, and ZnO was deposited in the channel over the course of 1 h and 40 min. Stylus profilometry (Bruker Dektak 150) was used to measure the thickness of ZnO across the channel. The maximum ZnO thickness was 150 nm at the center of the channel and dropped off to 0 nm at the corners of the channel. ZnO was sputtered to ensure ZnO deposition on all sides of the channel, thereby minimizing the impact of PDMS hydrophobicity on hydrothermal nanowire growth. The channels were annealed at 100°C overnight to improve ZnO seed surface morphology and subsequent nanowire growth.

2.2 ZnO Seed on PDMS Substrates

PDMS substrates were fabricated for two purposes in this work. First, it was necessary to explore the effect of PDMS thickness on the quality of the Raman signal because the crosslinked

polymeric nature of cured PDMS scatters light.[31] Results of this exploration informed the design of the PDMS channel used in this work. Second, thin PDMS substrates were fabricated to characterize SERS of melamine through PDMS. These substrates were designed to mimic the thickness of the PDMS channel wall through which spectra of crystal violet were acquired.

To explore the effect of light scattering through PDMS on the SERS signal quality, bare ZnO nanowires and Ag nanoparticle-decorated ZnO (Ag/ZnO) nanowires were constructed on thick and thin PDMS substrates, fabricated via soft lithography with Sylgard 184®. Substrate thickness was controlled by varying the PDMS volume placed into Pyrex® Petri dishes (95 mm diameter). 7.0 g of PDMS was poured into one Petri dish, and 1.4 g of PDMS was poured into another, targeting 1.0 and 0.2 mm PDMS thicknesses for thick and thin substrates, respectively. After oven-curing, PDMS squares of ~1 cm × 1 cm were cut from the center of each Petri dish to form substrates for sensor fabrication. The substrates were cleaned via the ALD-AMD method, and the thickness of each substrate was determined via stylus profilometry to be ~1.0 mm for the thick substrates and ~0.17 mm for the thin substrates. The discrepancy between the targeted thickness of 0.2 mm and the resultant thickness of 0.17 mm was caused by capillary action drawing PDMS up along the walls of the Petri dish. Subsequent substrates fabricated for SERS of melamine were fabricated with a controlled thickness by pouring PDMS between two glass slides with a single layer of 0.15-mm thick carbon tape as a spacer. This resulted in 0.15-mm thick PDMS substrates. Cleaned substrates were mounted in an e-beam deposition chamber (Thermionics, 150-0040). The chamber was pumped down to a vacuum of 5×10^{-6} Torr, and a 100-nm ZnO seed layer was deposited at a rate of ~0.1 Å/s. PDMS substrates were mounted in a plan configuration throughout ZnO deposition.

2.3 ZnO Nanowire Growth

The ZnO nanowire growth process is similar to that described in previous work.[11] ZnO nanowires were grown hydrothermally. PDMS channels and substrates with a ZnO seed were submerged in a 20-mM equimolar solution of zinc acetate dihydrate (Sigma Aldrich, BCBM3068V) and hexamethylenetetramine (Sigma Aldrich, MKBS8102V) in a Teflon reaction chamber. This chamber was placed in a preheated oven at 95°C for 2.5 h, after which the chamber was rapidly cooled under running water. The channels and substrates were washed of residual organics with DI water and then placed in the oven at 105°C for ~10 min to dry. Nanowires were grown only where the seed layer was deposited.

2.4 Ag Nanoparticle Formation

ZnO nanowires on PDMS substrates were decorated with Ag nanoparticles via e-beam deposition (Thermionics, 150-0040), as shown in Fig. 9. The nanowire substrates were mounted on a glancing-angle deposition apparatus, which rotates azimuthally at an angle during deposition. Glancing-angle deposition was used to ensure uniform coverage of the nanowire surfaces with Ag nanoparticles rather than e-beam deposition that is highly directional.[22] The angle of deposition was calculated by Eq. (1) to maximize the area of nanowire sides exposed to deposition while minimizing shadowing from adjacent nanowires. The nanowire length L_n and spacing D_n were estimated to be 320 and 76 nm, respectively. From these, an angle of $\theta_{\text{dep}} = \sim 13$ deg was calculated. The deposition chamber was depressurized to $\sim 5.0 \times 10^{-6}$, at which point Ag was deposited at a rate of ~0.1 Å/s to a nominal film thickness of 10 nm while the stage was rotated. This resulted in an effective film thickness (t_{eff}) ~2.2 nm on the sides of the nanowires as calculated by Eq. (2), where t_{nom} represents the nominal film thickness and θ_{dep} represents the angle of deposition specified above:

$$\theta_{\text{dep}} = \tan^{-1}(D_n/L_n), \tag{1}$$

$$t_{\text{eff}} = t_{\text{nom}} \sin(\theta_{\text{dep}}). \tag{2}$$

Ag nanoparticles were deposited in PDMS channels via e-beam deposition (Angstrom Amod Multimode Deposition System), as shown in Fig. 10. The nanowire substrates were mounted with a Kapton-tape mask such that only the channel was exposed on a stage at an angle of ~24 deg from the source crucible. The chamber was pumped down to a pressure

of $\sim 4.0 \times 10^{-6}$ Torr. Ag was deposited at a rate of ~ 0.1 Å/s to a nominal film thickness of 15 nm while the stage was rotated. This resulted in an effective film thickness (t_{eff}) of ~ 6.1 nm on the sides of the nanowires and ~ 13.7 nm on the bottom of the channel. This effective film thickness on the nanowire sides is within the range of 5 to 9 nm film thickness demonstrated in our previous work[35] to maximize SERS acquired with a 532-nm laser. The mask was designed to allow for Ag deposition only inside the channel. After deposition, the microchannel was heated to 50°C for 2 h to anneal the nanoparticles, which was shown in our previous work to greatly increase the surface enhancement.[35]

2.5 Microfluidic Fabrication

After the fabrication of Ag-decorated ZnO nanowires inside the microchannels, holes were punched at the inlet and outlet with a 2-mm disposable biopsy punch (Premier® Uni-Punch®), and they were placed in a plasma oxidation chamber (Harrick Plasma PDC-001) for 4 min to oxidize the PDMS surface. This enabled bonding to a glass slide (Fisherbrand® 12-550-A3). Tygon® tubing (ID: 0.020 in.; OD: 0.060 in.) was inserted at the inlet and outlet, and PDMS was used to seal the interface between the PDMS and tubing.

2.6 Characterization Techniques

Scanning electron microscopy images of bare and Ag-decorated ZnO nanowires were acquired with a Zeiss Merlin scanning electron microscope (Jena, Germany) in both plan and 45 deg configurations. These images were used to visually inspect nanowire and nanoparticle morphology. All image analysis was performed using ImageJ.

Photoluminescence (PL) spectra of ZnO nanowires were acquired to assess nanowire crystallinity using a thermoelectrically cooled (−40°C) CCD camera in a spectroscopy setup (HORIBA Jobin Yvon LabRAM 800HR). ZnO nanowire emissions were excited using a 325-nm He-Cd laser (Kimmon, 1 K series 200 mW, vertically polarized output measured at the laser head). PL spectra were acquired with a 15×-magnification objective lens (Thorlabs, LMU-15×-NUV, NA = 0.32) and detected in line with the laser normal to the substrate surface. Nanowires were oriented facing incident light. Five locations on each patch of nanowires were chosen, with a precision of 100 μm. At each location, a PL spectrum was acquired over a wavelength range of 340 to 700 nm. Each spectrum was the accumulation of four background-subtracted spectra, each taken with a 200-μm aperture and a 600-grooves/mm grating. The exposure time was 0.1 s, and the laser power was between 4.0 to 5.0 mW, as measured at the lens. The five spectra for each patch were averaged to produce a representative PL spectrum for each patch of nanowires within the channel.

To characterize the effect of PDMS-induced scattering on the spectral quality, SERS spectra of crystal violet in solution were acquired through Ag/ZnO and bare ZnO nanowires on 1.0- and 0.17-mm substrates to compare SERS and non-SERS spectra. These spectra were acquired using a CCD camera on the same spectroscopy setup as the PL measurements with a 532-nm laser (Ventus, 500 mW, horizontally polarized output measured at the laser head) and a 10×-magnification lens (Olympus, MPlan N Achromat, NA = 0.25). Raman scattering was collected in line with the laser normal to the substrate surface. PDMS substrates were affixed face down in a reservoir filled with 25 μM crystal violet, with the Ag-decorated and bare ZnO nanowires oriented away from the incoming laser light. Raman spectra were acquired over a range of 100 to 1800 cm^{-1}. Each Raman spectrum was the accumulation of two background-subtracted spectra, taken with a 20-s exposure time, a 200-μm aperture, and an 1800-grooves/mm grating. The laser power was 10.0 mW, measured at the turret. Raman spectra background was subtracted using a proprietary intelligent fitting algorithm developed by Renishaw.[36] The algorithm used an 11th order polynomial and a noise tolerance of 1.50. Spectra were smoothed using a Savitzky–Golay filter. Crystal violet was chosen for this purpose to facilitate detection due to its multiple strong Raman peaks where the PDMS Raman signal is weak. These spectra were intensity normalized using the 687-cm^{-1} PDMS peak.

There was concern that the ALD-AMD cleaning method would modify the Raman spectrum of the PDMS by introducing solvents into the PDMS. Curling of the substrates was observed after the cleaning process, presumably due to the presence of residual acetone and methanol. To address this concern, nine Raman spectra of a single PDMS substrate before cleaning were

acquired and averaged, using the same system and conditions detailed for the spectra acquired through thick and thin PDMS. After cleaning, Raman spectra were acquired at the same locations as before and averaged. These spectra were intensity normalized using the 488-cm^{-1} PDMS peak.

Raman spectra of melamine through 0.15-mm thick PDMS were acquired with the same system described above. Raman spectra used to quantify SERS were acquired in a range of 200 to 1800 cm^{-1} for two Ag-decorated ZnO nanowire substrates deposited on 150-μm-thick PDMS, hereafter referred to as S1 and S2. Each Raman spectrum acquired through S1 was the accumulation of four background-subtracted spectra, each taken with a 10-s exposure time. Each Raman spectrum acquired through S2 was the accumulation of eight background-subtracted spectra, each taken with a 1-s exposure time. All Raman spectra of melamine were acquired with a 200-μm aperture and a 600-grooves/mm grating. The laser power was 5 mW, measured at the turret. Raman spectra background was subtracted using an asymmetric least squares method and smoothed with a Savitzky–Golay filter.

Raman spectra of crystal violet injected into the SERS-integrated PDMS channel were acquired with a Thermo Scientific DXR Raman microscope (Waltham, Massachusetts, United States). A 532-nm diode-pumped, solid state laser was used with a 50× objective (Olympus, MPlan N Achromat, 0.75 NA) at a power of 10 mW as measured at the objective turret. These spectra were intensity normalized using the 488-μm PDMS peak.

Raman spectra were acquired through the PDMS channel "roof" bearing Ag/ZnO nanowires over a range of 100 to 1800 cm^{-1}. Each Raman spectrum was the accumulation of four background-subtracted spectra, each taken with a 60-s exposure time, a 50-μm slit aperture, and a 900-grooves/mm grating. The laser power was 10 mW, as measured at the objective, and Raman scattering was detected in-line with the laser normal to the surface of the sample. Raman spectra background were subtracted using a fifth order polynomial and smoothed with a Savitzky–Golay filter. These spectra were intensity normalized using the 488-μm PDMS peak.

To characterize the plasmonic properties of Ag nanoparticles, ultraviolet-visible-near infrared (UV-vis-NIR) extinction spectra were acquired using a Hitachi U-4100 spectrophotometer with an integrating sphere. Extinction spectra were acquired at a rate of 300 nm/min over a range of 350 to 850 nm, with the nanowire substrate oriented facing oncoming light.

3 Result and Discussion

3.1 Effect of Cleaning on PDMS Raman Spectrum

Because SERS-active nanostructures were fabricated on the PDMS surface of the microchannel, SERS will be performed through that PDMS wall. Because PDMS is porous, it is known to absorb multiple solvents used during the ALD-AMD cleaning process.[37,38] Indeed, curling of substrates was observed after cleaning, although subsequent placement of the substrates in a vacuum reduced this curling. It is essential that the Raman spectrum of PDMS be consistent to reliably extract the signal from dilute analytes, so Raman spectra were acquired before and after the cleaning process to determine whether solvent absorption had an observable effect on the spectrum of PDMS. A comparison of these Raman spectra exhibited only Raman peaks associated with PDMS, as shown in Fig. 11. No Raman peaks associated with any of the chemicals used in cleaning were observed. Thus the cleaning process demonstrably did not affect the Raman spectrum of PDMS.

3.2 ZnO Nanowire Characterization

To be suitable as a platform for SERS enhancements, ZnO nanowires must possess two characteristics: (1) the nanowires must be high quality, which means that they grow as single crystals with few defects, and (2) Ag/ZnO nanowires must possess uniform dimensional and structural properties, such as crystallinity. SEM images of nanowires (Fig. 12) show a dense bed of hexagonal nanowires, suggesting single crystallinity. A visual comparison of nanowires to remain bare and those to be decorated with Ag in Fig. 13 revealed no visible difference in the dimensionality or structure of the nanowires, providing validation for the quantification of SERS enhancements. Furthermore, SEM images revealed nanowires that are long enough to provide

a large surface area for SERS, but not so long as to induce nesting. Nesting would introduce shadowing during nanoparticle deposition, reducing nanoparticle coverage.

PL spectroscopy was used to assess the crystallinity of the ZnO nanowires. ZnO is a direct bandgap semiconductor with a band-edge emission of ~3.4 eV at room temperature,[14] which means that PL spectra of crystalline ZnO nanowires will have a sharp band-edge emission peak around 380 nm. Any native point defects within the crystalline structure, such as vacancies (missing atoms at regular lattice locations), interstitials (extra atoms occupying lattice interstices), or antisites (atoms occupying a lattice site where it does not belong), introduce transition levels within the bandgap, which induce emissions at wavelengths in the visible region.[39] This defect emission is very broad compared with the band-edge emission, and the ratio of band edge to defect emission in ZnO nanowires is an indicator of the nanowires' crystallinity.[40] PL spectra of the nanowires in Fig. 14 exhibit very little defect emission and very strong band-edge emission, providing further evidence of high crystallinity with few defects. Although the band-edge emission peak at 392 nm is shifted slightly for nanowires grown on PDMS versus the band-edge emission of 380 nm previously reported for nanowires similarly grown on fused silica,[40] the ratio of band edge to defect emission remained similarly large. A comparison of the PL spectra for nanowires to remain bare (non-SERS) and those to be decorated with nanoparticles (SERS) revealed minor variations. Five PL spectra were acquired of each population and averaged. The band-edge and defect emission for non-SERS exhibited a relative standard deviation (RSD) of 2.4% and 3.4%, respectively, whereas the SERS nanowires exhibited an RSD of 5.9% and 3.5% for band-edge and defect emission, respectively. The average band-edge peak intensity for non-SERS nanowires was within 10% of that for SERS nanowires, indicating that the nanowire populations had similar nanowire density and dimensions. The ratio between band-edge emission and defect emission in the visible region was ~56.9 for SERS nanowires and ~46.4 for non-SERS nanowires, indicating that both populations were highly crystalline with few defects. These features indicated that light would interact with both nanowire populations similarly, enabling high confidence in the comparison of non-SERS to SERS spectra.

To explore the possibility of patterning ZnO nanowire growth by patterning the ZnO seed layer deposition, a partially shielded PDMS substrate was deposited with a 100-nm seed layer, in which nanowires were hydrothermally grown. UV-Vis-NIR spectra of the seeded and nonseeded portions of the substrate (Fig. 15) indicated nanowire growth on the seeded portion of the substrate and negligible nanostructure formation on the unseeded portion.

3.3 Ag Nanoparticle Deposition Characterization

ImageJ analysis of the SEM images of bare nanowires grown on PDMS substrates revealed an approximate nanowire height of 320 nm and approximate interwire spacing of 76 nm. Applying these values in Eq. (1) resulted in an Ag deposition angle of ~13 deg. SEM image of the nanowires after nanoparticle deposition revealed a dense population of nanoparticles on the nanowire sides (Fig. 13). UV-Vis-NIR extinction spectra of Ag/ZnO nanowires before and after Ag deposition revealed a plasmon absorption peak centered at ~450 nm (Fig. 16).

3.4 Effect of PDMS Thickness on Surface Enhancement

To quantify SERS, Raman spectra were acquired of a 25-μM solution of crystal violet dye in DI water through both bare ZnO nanowires and Ag/ZnO nanowires for both PDMS thicknesses. Representative examples of these spectra are shown in Fig. 2. The SERS intensity was greater for thin PDMS than for thick. This difference was presumably due to increased light scattering through thick PDMS, resulting in less Raman-scattered light reaching the detector. Crystal violet has several strong bands in the fingerprint region of its Raman spectra that can be decoupled from the strong Raman peaks of PDMS, shown in Fig. 11. Furthermore, plasmonic nanoparticles used for SERS are separated from PDMS by at least 100 nm, which was the thickness of the ZnO seed layer. This is more than enough to ensure that the PDMS Raman contributions do not experience significant surface enhancements. Enhancement was quantified for 13 individual crystal violet Raman peaks distinguishable from the PDMS background in non-SERS spectra, tabulated with their raw enhancement through thick and thin PDMS in Table 1. Table 2 provides the vibrational modes for the Raman bands of PDMS. Raw enhancement, simply the difference in peak intensity between SERS and non-SERS spectra, ranged from an average of 2.2-fold for spectra taken

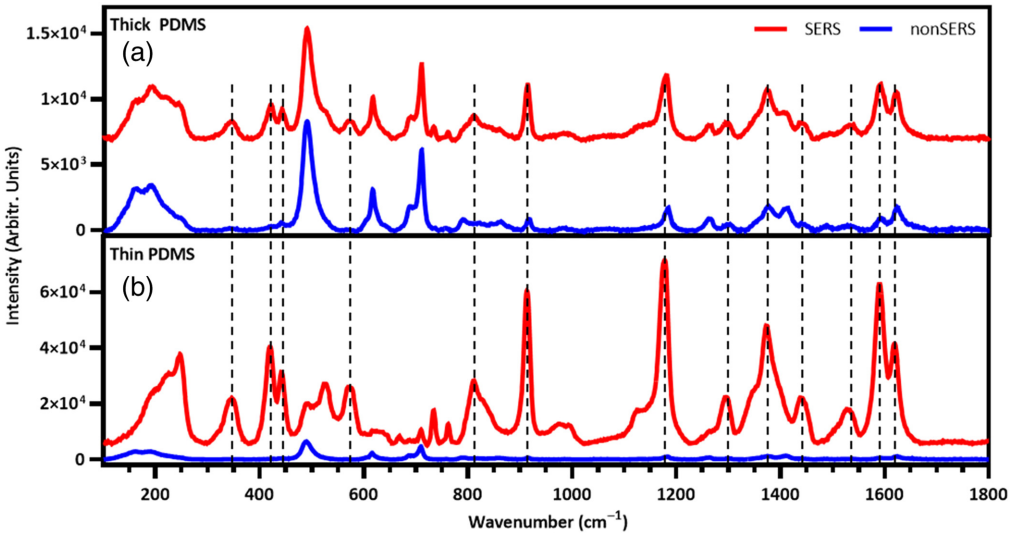

Fig. 2 SERS (red) and non-SERS (blue) Raman spectra of crystal violet through (a) thick and (b) thin PDMS, demonstrating the ability to perform SERS spectroscopy through a PDMS wall, as well as the importance of PDMS thickness on the magnitude of enhancement. CV peaks identified by dotted lines.

Table 1 Crystal violet Raman peaks used to compare the surface enhancement through thick versus thin PDMS.

Raman band (cm^{-1})	Thick PDMS (≈ 1.0 mm)	Thin PDMS (≈ 0.17 mm)
345	2.81	300.17
420	3.63	284.76
441	2.45	74.34
571	2.41	292.79
810	2.17	86.42
915	2.42	111.04
1175	2.47	58.87
1300	1.57	80.21
1374	1.91	43.04
1445	1.55	84.25
1529	1.26	129.17
1592	2.25	116.60
1621	1.95	35.34

through thick (~1 mm) PDMS to an average of 130-fold for spectra taken through ~0.17-mm thick PDMS, as shown in Fig. 3, demonstrating the impact that PDMS thickness has on not only the SERS signal strength, but also the magnitude of enhancement observed. Although more PDMS thicknesses would be required to establish a relationship between PDMS thickness and surface enhancement, these data demonstrate that enhancement is inversely related to PDMS thickness. Thus it is vital to control the thickness of the PDMS cap through which analysis is performed. Multiple parameters must be considered to optimize PDMS thickness to maximize

sensing reliability. First, PDMS thickness must be counterbalanced by the channel's ability to withstand fluidic pressure without inappropriate deformation or rupture. The PDMS cap cannot be made so thin that it ruptures when samples are injected. Second, PDMS thickness must be uniform across the sensor area as well as from sensor to sensor. Uniform thickness is essential to reliable sensing.

3.5 Surface-Enhanced Raman Spectroscopy of Melamine Through PDMS Substrates

After demonstrating the viability of SERS through thin PDMS with crystal violet, SERS spectra were acquired of melamine solutions in DI water using SERS substrates fabricated on ~0.15-mm thick PDMS substrates. Two substrates, hereafter named P1 and P2, were fastened upside down to a reservoir, so Raman spectra were acquired through the PDMS substrate. Raman spectra were acquired of μM concentrations of melamine in DI water (1, 2, 3, 4, and 6 μM for P1; 2, 4, 6, 8, 10, and 12 μM for P2). Although the characteristic peak of melamine at 691 cm^{-1} is coincident with the PDMS peak at 703 cm^{-1} associated with Si-C symmetric stretching and CH_3 bending, multiple melamine peaks are visible even at concentrations of 1 and 2 μM for both substrates. Six melamine peaks other than the 691-cm^{-1} peak were identified in the spectra plotted in Fig. 3 that could be assigned vibrational modes, as tabulated in Table 3.[46,47] Importantly, the lowest concentrations detected are well below the 7.93-μM limit set by the Codex Alimentarius, demonstrating the efficacy of SERS sensing of melamine through PDMS.

SERS spectra exhibited substrate-to-substrate variation, with spectra from P2 generally having a greater melamine signal than P1, as illustrated by direct comparisons of the signals generated by 2, 4, and 6 μM concentrations of melamine shown in Fig. 3. Additionally, the signal intensity exhibited point-to-point variability, with spots on both substrates generating more melamine signal than other spots. This effect is likely due to variation in nanowire density caused by the hydrophobicity of PDMS inhibiting precursor flow around the ZnO seed during hydrothermal nanowire growth. This variability in nanowire growth would cause variability in the effective surface area. The ratios of melamine peak intensity to PDMS peak intensity at 488 cm^{-1} shown in Fig. 17 were averaged for each melamine peak across all concentrations measured for each substrate. For both substrates, the melamine to PDMS peak ratios followed the same trends with increasing concentration. Furthermore, the ratio of the 1596- to 845-cm^{-1} melamine peaks, shown in Fig. 18, remained consistent between substrates and across melamine concentrations, lending confidence that SERS can be used to reliably and consistently sense melamine through PDMS once device nanowire fabrication is standardized. In addition to variation across substrates, Raman spectra acquired at the same location on a single substrate exhibited varied intensity from measurement to measurement. It was observed that a Raman spectrum

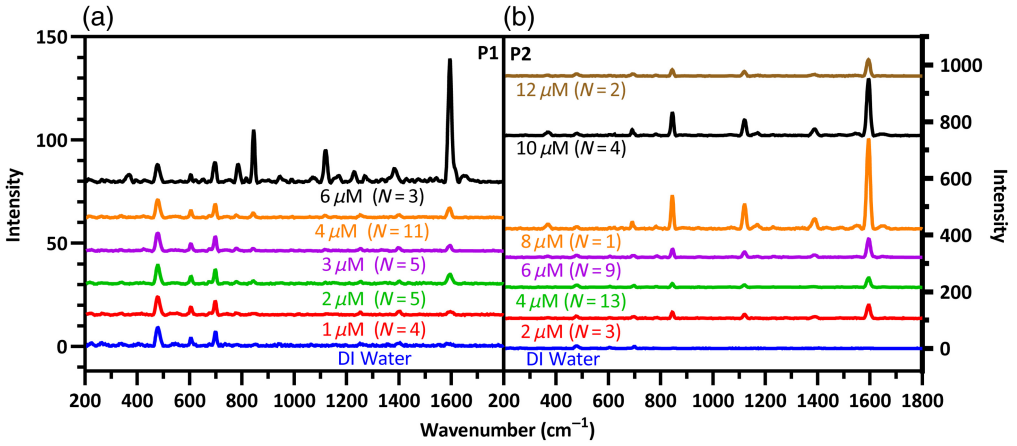

Fig. 3 SERS spectra of melamine in DI water, acquired through (a) P1 and (b) P2. Number of spectra acquired for each concentration through each substrate in parentheses.

taken immediately after the introduction of a melamine solution would exhibit little-to-no melamine signal. However, after the substrate was manually disturbed, strong melamine signal would appear in subsequent Raman spectra. This phenomenon is likely due to the hydrophobicity of nanowire beds preventing infiltration of the melamine solution. Disturbing the substrates allows the melamine solution to infiltrate the bed of nanowires, enabling much a stronger melamine signal. However, this infiltration was inconsistent.

3.6 Microchannel Mold Design and Fabrication

Based on the comparison between surface enhancement through thick and thin PDMS, it became apparent that a thin microchannel wall would be vital for successful SERS detection of trace analytes. Thus it was necessary to design a microchannel mold that would enable the fabrication of channels able to facilitate such sensitive SERS. The mold was designed with a base and lid as shown in Fig. 4, which would be fitted onto the base after PDMS was poured into the mold. The mold was designed such that channels fabricated would be z-shaped channels with a 2-mm width in the center portion to facilitate subsequent nanostructure fabrication. The channel's top wall was designed to be thick enough at the inlet and outlet to support tubing, but thin enough at 0.10 mm to enable sensitive SERS sensing with minimal PDMS interference. The channel's top wall was also designed such that the thicker portions would be far enough apart to allow for high-magnification objectives with short working distances close enough to focus on the SERS-active surface. The channel was designed with the z-shaped structure, ~7 mm long at the center, to enable Raman spectra to be acquired at multiple points along the center portion. The mold was milled from aluminum in the machine shop of the Physics Department at Vanderbilt University. As a function of the milling process, small ridging occurred on the surface of the mold lid, which could interfere with SERS sensing through the top wall. To combat this, a glass slide was cut to fit the center portion of the lid and affixed with Kapton tape to the mold lid. Glass spacers were also cut and similarly affixed to the ends of the lid, which would rest on the base, to maintain the designed thickness of the PDMS cap.

3.7 Fabricating SERS Substrates Inside PDMS Channels

Several channels were sputtered with a ZnO seed layer and grown with nanowires. PL spectra of the nanowires inside the channels, shown in Fig. 19, exhibited a large band-edge emission and minimal visible emission, indicating high crystallinity with few defects. The intensity of the band-edge emission varied from channel to channel, as shown in Fig. 19, which indicates variability in the amount of ZnO present in the channels. As exhibited by Fig. 20, nanowire density and dimensions varied from channel to channel. Nanowire formation was, in general, sparser for sputtered seed layers versus e-beam deposited seed layers as exemplified by a comparison of nanowire density between Figs. 12 and 20. This variability demonstrates that sputtered ZnO does not result in uniform nanowire growth, indicating that another means of combating PDMS hydrophobicity should be explored. One possible way to do so would be to make channels with a copolymer consisting of PDMS and poly(ethylene oxide), which has been shown to

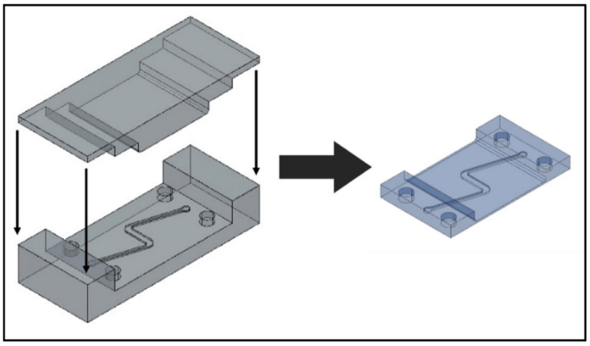

Fig. 4 AutoCAD drawing of the microchannel mold designed to enable sensitive SERS through the top channel wall along with the resultant microchannel.

improve hydrophilicity.[48] Making the channels hydrophilic should improve the precursor flow at an e-beam deposited ZnO seed layer, which would make nanowire growth and density more uniform. In addition, although Kapton tape was sufficient to mask the channels described in this work for nanowire growth, photolithography has been successfully implemented for selective-area nanowire growth[49] and would enable greater precision and flexibility in the device design.

Channel 4 in Fig. 20 exhibited the most consistent nanowire growth and was selected for further development. The SEM image of the channel taken before [Fig. 5(a)] and after Ag deposition [Fig. 5(b)] confirmed the growth of highly crystalline nanowires inside the channel. The nanowires shown in Fig. 5 are sparser than those in Figs. 12 and 13. This sparser formation is likely due to the use of sputtered seed layers. Mitigating the hydrophobicity of the channel as discussed above will facilitate the use of e-beam seed deposition, thereby making future nanowire growth inside channels more consistent with that demonstrated on PDMS substrates. The UV-Vis spectrum of the Ag/ZnO nanowires in the channel (Fig. 6) exhibited a clear plasmon peak at ~515 nm and shoulder at ~600 nm. This is likely because of the dual size populations of Ag nanoparticles deposited on the nanowire sides and the floor of the channel as is exhibited by SEM of the Ag/ZnO nanowires in Fig. 5(b). The nanoparticles on the floor of the channel have an estimated average diameter of ~28 nm, whereas the nanoparticles on the sides of the nanowires had an estimated average diameter of ~18 nm, as measured by ImageJ. This result corresponds with the previously reported correlation between peak plasmon wavelength and silver nanoparticle size.[35] The plasmon emission peaked at ~515 nm, close to the 532-nm laser line and extended well past the end of the fingerprint region at ~590 nm, making the channel suitable for SERS. Subsequently, the channel was completed by binding the PDMS to a glass slide, and tubing was inserted at the inlet and outlet.

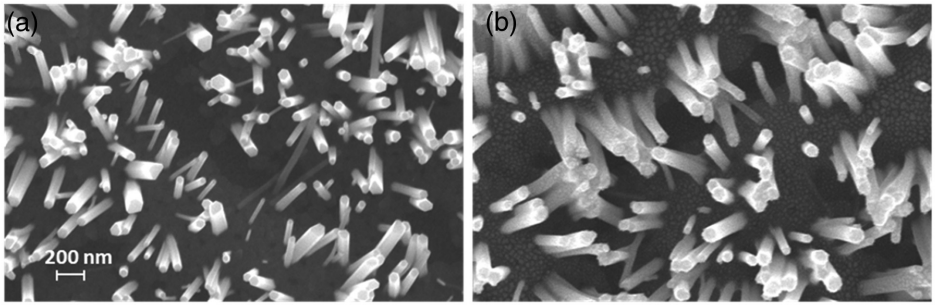

Fig. 5 SEM images of ZnO nanowires (a) before and (b) after deposition and annealing of Ag, demonstrating nanowire growth and Ag nanoparticle formation.

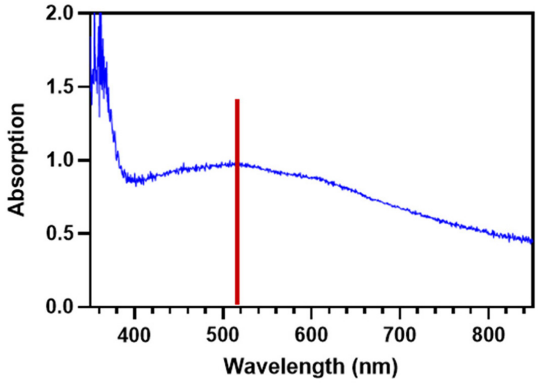

Fig. 6 UV-Vis-NIR spectrum of ZnO nanowires decorated with Ag nanoparticles after annealing. The red vertical line indicates a plasmon peak at 515 nm.

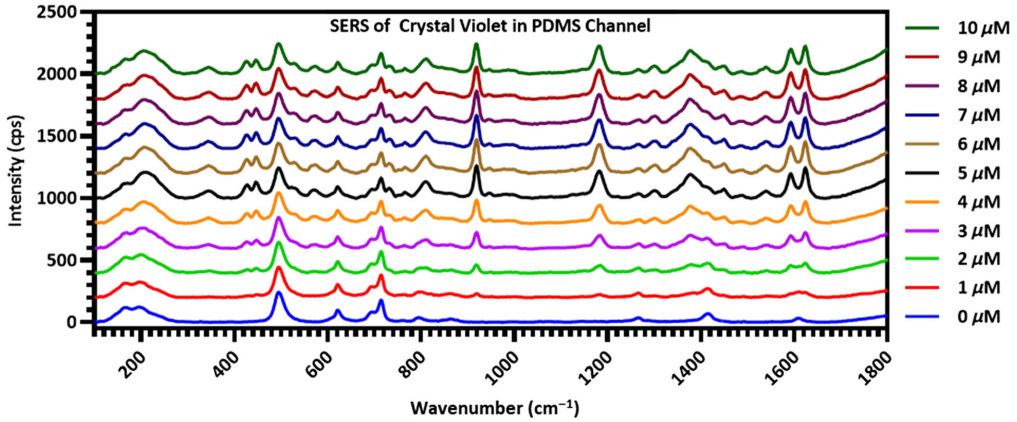

Fig. 7 Raman spectra of crystal violet solutions taken inside a fabricated channel, in concentrations ranging from 1 to 10 μM with a DI water control.

3.8 Surface-Enhanced Raman Spectroscopy of Crystal Violet in Channel

Crystal violet was used to characterize an SERS detection in the completed channels because crystal violet has multiple strong peaks between 900 and 1200 cm^{-1}, where the Raman of PDMS is relatively weak. Raman spectra were acquired of 10 crystal violet solutions in DI water ranging from 1 to 10 μM concentrations in 1 μM increments, with a DI-water control (Fig. 7). Before each solution was syringed through the channel, it was flushed with DI water, and the Raman spectra were all acquired at the same location along the channel. There are two strong crystal violet peaks in particular that are not near any PDMS peaks: the $C-C_{center}-C$ bending peak at 917 cm^{-1} and the $C-C_{center}-C$ asymmetric stretching peak at 1175 cm^{-1}. These peaks were not present in the control spectrum with no crystal violet, but clearly visible at a 1-μM concentration. These crystal violet peaks exhibited a steady increase in intensity through the 5-μM concentration, as illustrated in Fig. 21. From 6 to 10 μM, however, the peak intensity reached an asymptotic maximum. Raman spectra taken of the sensing surface after crystal violet solutions were flushed from the channel with DI water exhibited crystal violet peaks, meaning the leveling off of the Raman signal was likely due to accumulation of crystal violet adsorbed on the sensing surface.

4 Conclusions

This work demonstrated a facile technique to fabricate physically deposited Ag nanoparticle-decorated ZnO nanowires inside fluidic channels, allowing microfluidic SERS sensing to benefit from dense Ag nanoparticle formation from e-beam deposition. Through careful design and fabrication of fluidic channels to minimize spectral interference from PDMS, μM concentrations of crystal violet and melamine were detected, demonstrating the ability of the fluidic device to detect relevant concentrations of melamine. By further improvement on the SERS-active substrate fabrication process, it is expected that this process will provide the reliable and sensitive detection of melamine in SERS-active microfluidic devices.

5 Appendix

Tables 2 and 3 and Figures 8–21 in the Appendix provide supplementary information that supports the results and discussion of this work. These materials are intended for readers seeking additional justification for the conclusions proposed and to assist in the replication of these studies.

Table 2 Vibrational modes of PDMS in the fingerprint region: γ, torsion; δ, bending; v, stretching; σ, scissoring; ρ, rocking; s, symmetric; as, asymmetric; $\perp$, out-of-plane; and $\|$, in-plane.

Raman band (cm^{-1})	Vibrational modes	References
160	$\gamma_{as}(C-Si-C)$	41 and 42
188	$\delta(C-Si-C)/\delta(C-Si-O)/\gamma_s(C-Si-C)/\rho(C-Si-C)/\sigma(C-Si-C)$	41–43
488	$v_s(Si-O-Si)$	41–45
615	$v(Si-O-Si)/v(Si-C)$	41
646	$\rho_{as}(Si-C_3)$	45
687	$v(Si-C)/\rho(C-H_3)$	41–43
708	$v\text{-}s(Si-C)/\delta(C-H_3)$	41, 44, and 45
754	$\rho(C-H3)/\rho_s(Si-C3)/v(Si-C)$	41, 43, and 45
787	$\rho_{as}(C-Si-C)/v_{as}(C-Si-C)/\rho(C-H_3)$	41, 42, 44, and 45
845	$\rho_{as}(C-Si-C)$	45
859	$\rho(C-Si-C)/\rho(C-H_3)$	41, 42, 44, and 45
882	$\rho_{as}(Si-C_3)/\rho_{as}(C-Si-C)$	45
1088	$v_{as}(Si-O-Si)$	45
1262	$\delta_s(C-H_3)/\delta(C-H_2)$	41, 42, 44, and 45
1411	$\delta_{as}(C-H_3)/\delta(C-H_2)/\sigma(C-H_2)$	41–45

Table 3 Selected vibrational modes of melamine in the fingerprint region: γ, torsion; δ, bending; v, stretching; σ, scissoring; s, symmetric; and $\perp$, out-of-plane.

Raman band (cm^{-1})	Vibrational modes	References
380	$\delta(C-N)$	46 and 47
691	Ring breathing	46 and 47
845	$\delta_\perp$(ring)	46 and 47
1235	$\delta(N-H)$	47
1390	$\sigma(NH_2)/\nu(C-N)/\delta_s$(ring)	47
1595	$\delta(NH_2)/\delta(N-C-N)$	46

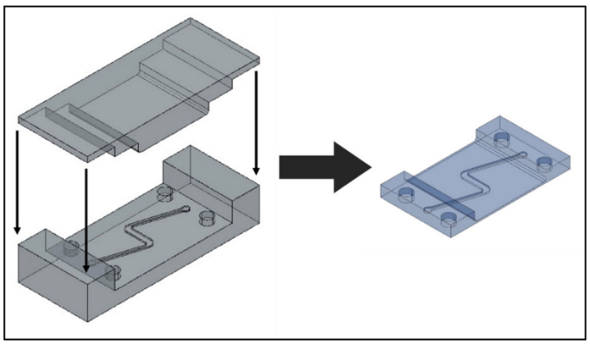

Fig. 8 Microchannel mold, designed in AutoCAD to minimize the PDMS spectral interference.

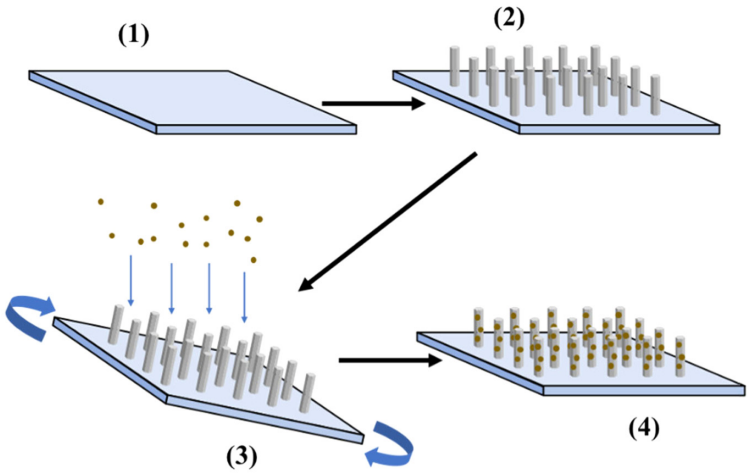

Fig. 9 Illustration of the Ag/ZnO nanoprobe fabrication process for PDMS substrates: (1) deposit 100-nm ZnO seed layer on PDMS, (2) hydrothermally grow ZnO nanowires, and (3) deposit Ag on the nanowires on an azimuthally rotated sample to get (4) a finished Ag/ZnO nanoprobe.

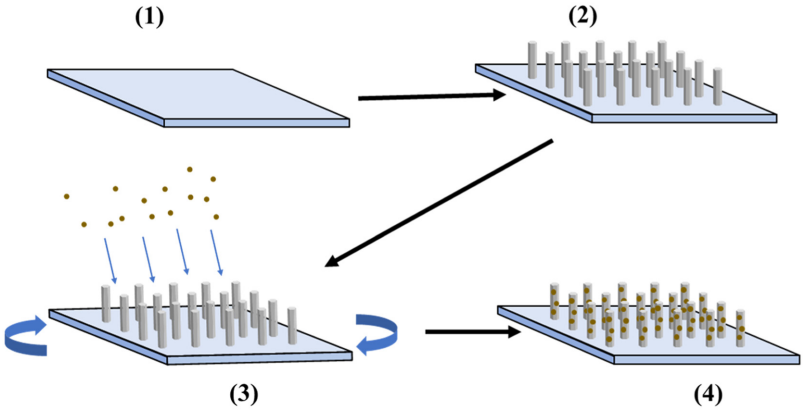

Fig. 10 Illustration of the Ag/ZnO nanoprobe fabrication process for PDMS channels: (1) deposit 100-nm ZnO seed layer on PDMS, (2) hydrothermally grow ZnO nanowires, and (3) deposit Ag from an angle on the nanowires inside a rotated channel to get (4) a finished Ag/ZnO nanoprobe.

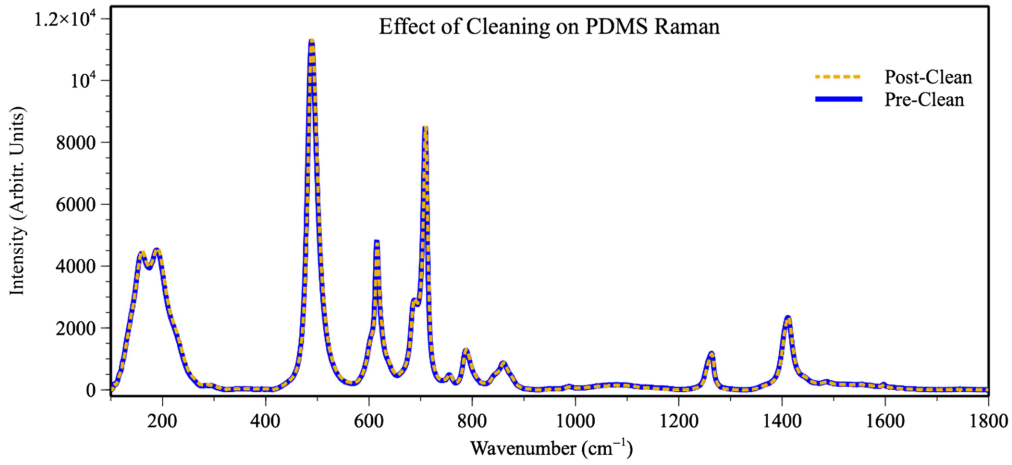

Fig. 11 Raman spectra of PDMS before and after the ALD-AMD cleaning process, demonstrating no spectral effects due to cleaning.

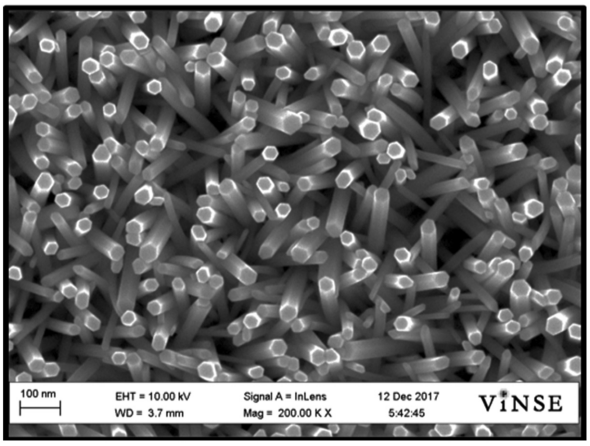

Fig. 12 SEM image of bare ZnO nanowires, exhibiting highly crystalline nanowires.

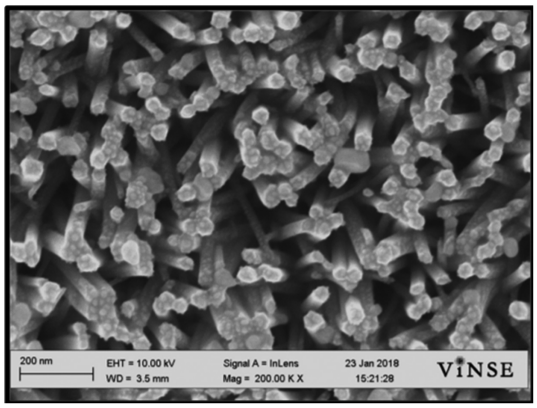

Fig. 13 SEM image of ZnO nanowires after Ag nanoparticle decoration, demonstrating dense nanoparticle formation on the sides of nanowires.

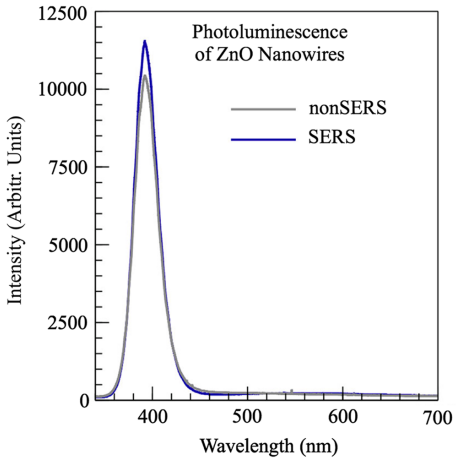

Fig. 14 PL of ZnO nanowires to be decorated with Ag nanoparticles and those to remain bare, demonstrating the highly crystalline nature of the nanowires and the similarity between the two sets of nanowires.

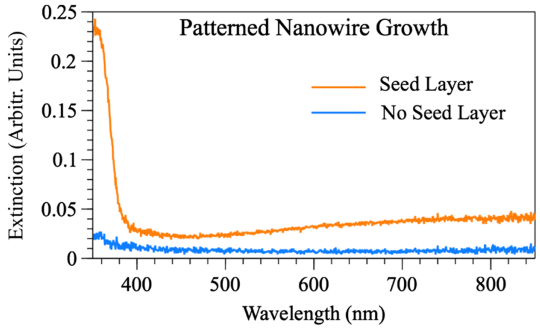

Fig. 15 UV-Vis-NIR extinction spectra after nanowire growth of the seeded and nonseeded portions of a patterned PDMS substrate, demonstrating the ability to pattern nanowire growth on PDMS by patterning the seed layer.

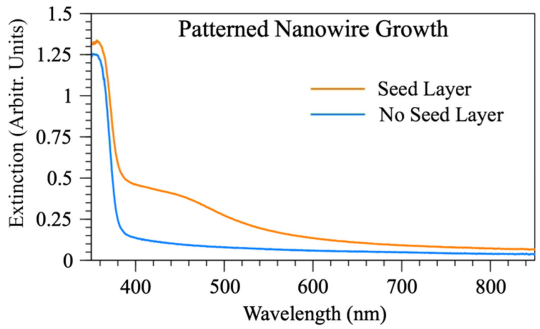

Fig. 16 UV-Vis-NIR extinction spectra of Ag/ZnO nanoprobe before and after Ag deposition, demonstrating the formation of plasmons, centered at ~450 nm.

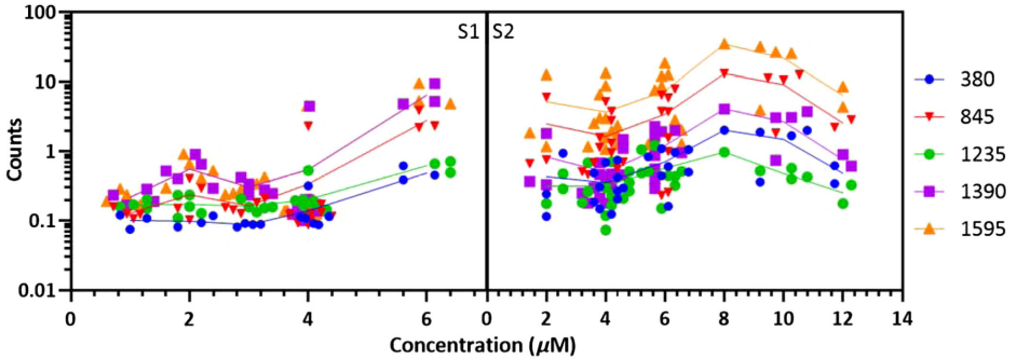

Fig. 17 Ratios of each melamine peak with the PDMS peak at 488 cm^{-1} for each substrate, illustrating the consistency of melamine peak intensities relative to the overall signal intensity for each measurement.

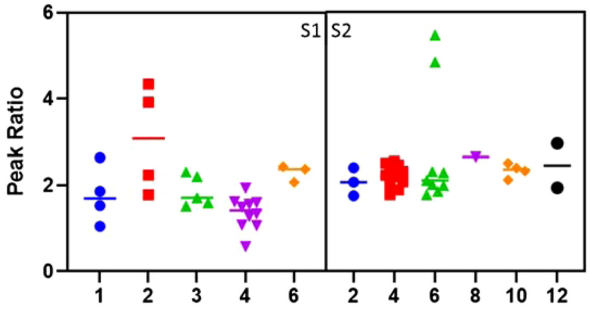

Fig. 18 Ratios of melamine peaks at 1595 to 845 cm^{-1} for each melamine concentration measured for each substrate, illustrating the internal signal consistency for all concentrations measured and across substrates.

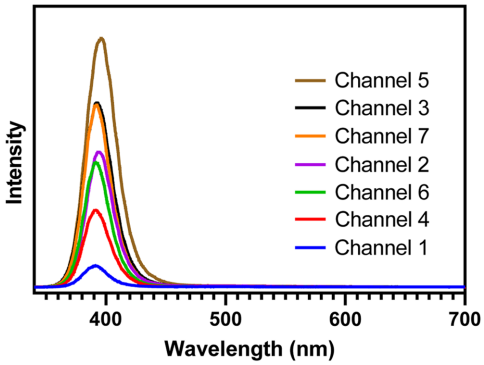

Fig. 19 Photoluminescence spectra of ZnO nanowires in seven different PDMs channels, demonstrating variability in ZnO nanowire structure, though each still exhibits high crystallinity with few defects.

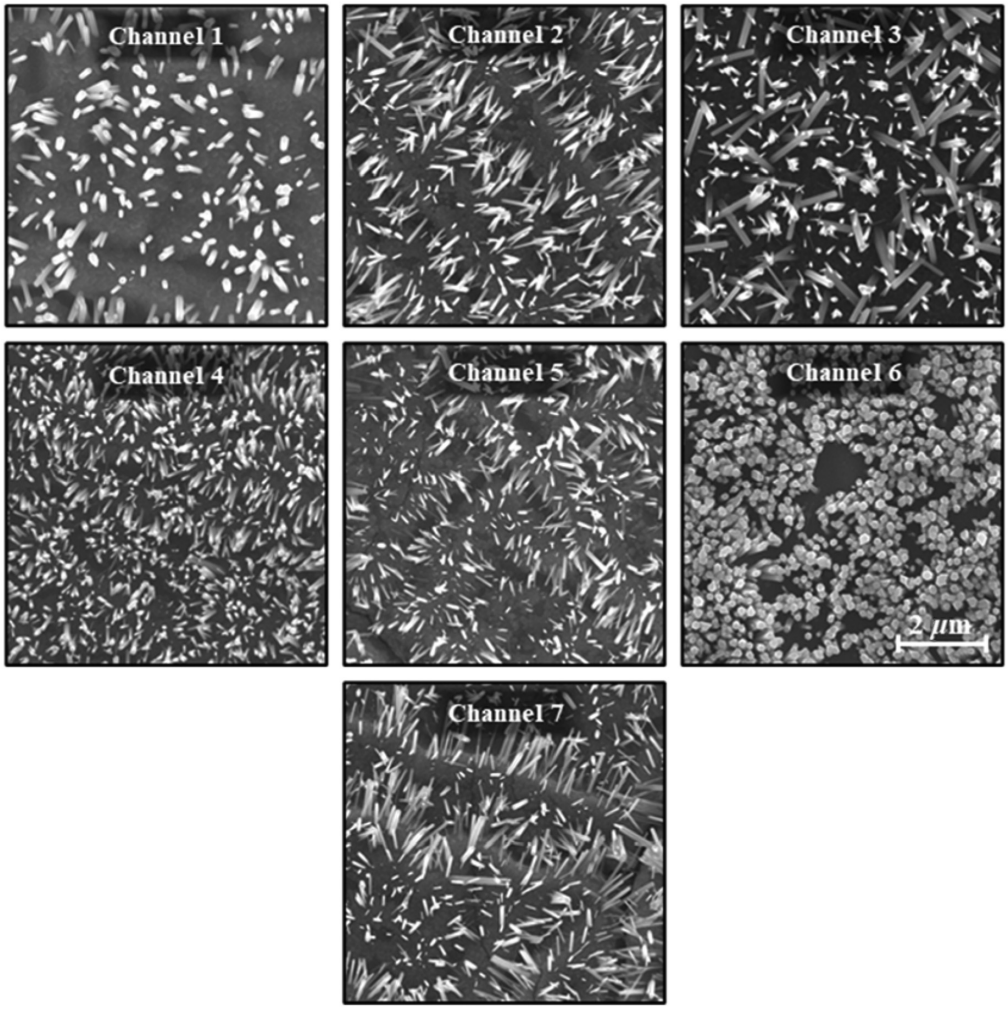

Fig. 20 SEM images of nanowires within PDMS channels on sputtered ZnO seed layers, illustrating the variability of nanowire growth on sputtered seed layers.

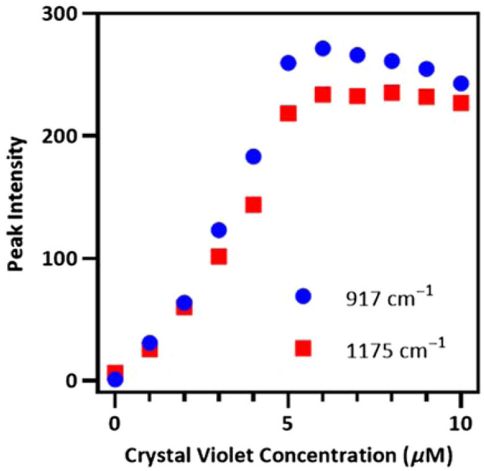

Fig. 21 Intensity of two crystal violet peaks as a function of increasing crystal violet concentrations.

Disclosures

The authors have no conflicts of interest to declare.

Code and Data Availability

Code sharing is not applicable to this article as no new code was created. All data in support of the findings of this paper are available within the article or in the Appendix material.

Acknowledgments

A.L. Cook acknowledged support from the National Science Foundation Graduate Research Fellowship Program (No. 1445197). A.L. Cook and T.D. Giorgio also acknowledged support from the Congressionally Directed Medical Research Program and Peer Reviewed Medical Research Program (No. W81XWH-18-1-0412). The authors would like to thank Eugene Collins and Akira Ueda at Fisk University for the use of their facilities and equipment. The authors also would like to thank the Vanderbilt Institute of Nanoscale Science and Engineering for the use of their cleanroom and equipment and Bill Martinez for his assistance and training in the use of VINSE equipment. Finally, the authors would like to thank Andrea Locke for her input in the development and execution of this work.

References

1. J. Guo et al., "Preparation and application of microfluidic SERS substrate: challenges and future perspectives," *J. Mater. Sci. Technol.* **37**, 96–103 (2020).
2. K. B. Kim et al., "Dynamic preconcentration of gold nanoparticles for surface-enhanced Raman scattering in a microfluidic system," *Small* **8**, 378–383 (2012).
3. H. Hwang et al., "In situ dynamic measurements of the enhanced SERS signal using an optoelectrofluidic SERS platform," *Lab Chip* **11**, 2518–2525 (2011).
4. C. Novara et al., "Surface-enhanced Raman spectroscopy on porous silicon membranes decorated with Ag nanoparticles integrated in elastomeric microfluidic chips," *RSC Adv.* **6**, 21865–21870 (2016).
5. Y.-J. Oh and K.-H. Jeong, "Optofluidic SERS chip with plasmonic nanoprobes self-aligned along microfluidic channels," *Lab Chip* **14**, 865–868 (2014).
6. H.-Y. Wu and B. T. Cunningham, "Point-of-care detection and real-time monitoring of intravenously delivered drugs via tubing with an integrated SERS sensor," *Nanoscale* **6**, 5162–5171 (2014).
7. H. Pu, W. Xiao, and D.-W. Sun, "SERS-microfluidic systems: a potential platform for rapid analysis of food contaminants," *Trends Food Sci. Technol.* **70**, 114–126 (2017).
8. I. J. Jahn et al., "Surface-enhanced Raman spectroscopy and microfluidic platforms: challenges, solutions and potential applications," *Analyst* **142**, 1022–1047 (2017).
9. J.-A. Huang et al., "SERS-enabled lab-on-a-chip systems," *Adv. Opt. Mater.* **3**, 618–633 (2015).
10. Y. Xie et al., "In situ fabrication of 3D Ag@ZnO nanostructures for microfluidic surface-enhanced Raman scattering systems," *ACS Nano* **8**, 12175–12184 (2014).

11. A. L. Cook et al., "Sensing trace levels of molecular species in solution via zinc oxide nanoprobe Raman spectroscopy," *J. Raman Spectrosc.* **48**, 1116–1121 (2017).
12. X. Liu et al., "Aligned ZnO nanorods: a useful film to fabricate amperometric glucose biosensor," *Colloids Surf. B Biointerfaces* **74**, 154–158 (2009).
13. H.-Y. Shin et al., "Giant enhancement of the Raman response due to one-dimensional ZnO nanostructures," *Nanoscale* **6**, 14622–14626 (2014).
14. A. Janotti and C. G. Van de Walle, "Fundamentals of zinc oxide as a semiconductor," *Rep. Prog. Phys.* **72**, 126501–126530 (2009).
15. P. Yang et al., "Controlled growth of ZnO nanowires and their optical properties," *Adv. Funct. Mater.* **12**, 323–331 (2002).
16. P.-H. Lei and C.-H. Cheng, "Fabrication of Ag nanoparticle/ZnO thin films using dual-plasma-enhanced metal-organic chemical vapor deposition (DPEMOCVD) system incorporated with photoreduction method and its application," *Mater. Sci. Semicond. Process.* **57**, 220–226 (2017).
17. Z. Yi et al., "Fabrication of well-aligned ZnO@Ag nanorod arrays with effective charge transfer for surface-enhanced Raman scattering," *Surf. Coat. Technol.* **324**, 257–263 (2017).
18. Y. Wang et al., "Direct observation of surface-enhanced Raman scattering in ZnO nanocrystals," *J. Raman Spectrosc.* **40**, 1072–1077 (2009).
19. Z. Kang et al., "Enhanced photoelectrochemical property of ZnO nanorods array synthesized on reduced graphene oxide for self-powered biosensing application," *Biosens. Bioelectron.* **64**, 499–504 (2015).
20. G. Barbillon, "Fabrication and SERS performances of metal/Si and Metal/ZnO nanosensors: a review," *Coatings* **9**, 86 (2019).
21. Y. S. Park and J. R. Schneider, "Index of refraction of ZnO," *J. Appl. Phys.* **39**, 3049–3052 (1968).
22. D. C. Mayo et al., "Surface-plasmon mediated photoluminescence from Ag-coated ZnO/MgO core–shell nanowires," *Thin Solid Films* **553**, 132–137 (2014).
23. W. Ji et al., "Enhanced Raman scattering by ZnO superstructures: synergistic effect of charge transfer and Mie resonances," *Angew. Chem.* **131**, 14594–14598 (2019).
24. B. K. Gale et al., "A review of current methods in microfluidic device fabrication and future commercialization prospects," *Inventions* **3**, 60 (2018).
25. G. S. Fiorini and D. T. Chiu, "Disposable microfluidic devices: fabrication, function, and application," *Biotechniques* **38**, 429–446 (2005).
26. K. Ren, J. Zhou, and H. Wu, "Materials for microfluidic chip fabrication," *ACC. Chem. Res.* **46**, 2396–2406 (2013).
27. Z. Li, X. Huang, and G. Lu, "Recent developments of flexible and transparent SERS substrates," *J. Mater. Chem. C* **8**, 3956–3969 (2020).
28. S. H. Lee et al., "Control of the ZnO nanowires nucleation site using microfluidic channels," *J. Phys. Chem. B* **110**, 3856–3859 (2006).
29. M. Ladanov et al., "Microfluidic hydrothermal growth of ZnO nanowires over high aspect ratio microstructures," *Nanotechnology* **24**, 375301 (2013).
30. Y. Zhang et al., "Gold and silver nanoparticle monomers are non-SERS-active: a negative experimental study with silica-encapsulated Raman-reporter-coated metal colloids," *Phys. Chem. Chem. Phys.* **17**, 21120–21126 (2015).
31. S. Seiffert et al., "Reduced UV light scattering in PDMS microfluidic devices," *Lab Chip* **11**, 966–968 (2011).
32. H. Mao et al., "Microfluidic surface-enhanced Raman scattering sensors based on nanopillar forests realized by an oxygen-plasma-stripping-of-photoresist technique," *Small* **10**, 127–134 (2014).
33. Q.-Q. Meng et al., "Figure of merit enhancement of a surface plasmon resonance sensor using a low-refractive-index porous silica film," *Sensors* **17**, 1846 (2017).
34. A. M. Giovannozzi et al., "Rapid and sensitive detection of melamine in milk with gold nanoparticles by Surface Enhanced Raman Scattering," *Food Chem.* **159**, 250–256 (2014).
35. A. L. Cook et al., "Optimization of electron beam-deposited silver nanoparticles on zinc oxide for maximally surface enhanced Raman spectroscopy," *Nanoscale Adv.* **3**, 407–417 (2021).
36. *Renishaw: Intelligent Background Removal*, Renishaw (2021).
37. C. V. Rumens et al., "Swelling of PDMS networks in solvent vapours; applications for passive RFID wireless sensors," *J. Mater. Chem. C* **3**, 10091–10098 (2015).
38. T.-M. Durďáková et al., "Swelling and plasticization of PDMS and PTMSP in methanol and dimethyl carbonate vapors and liquids: volume, mechanical properties, Raman spectra," *Polymer* **188**, 122140 (2020).
39. A. Galdámez-Martinez et al., "Photoluminescence of ZnO nanowires: a review," *Nanomaterials* **10**, 857 (2020).
40. D. C. Mayo et al., "Zinc oxide nanowire gamma ray detector with high spatiotemporal resolution," *Proc. SPIE* **9737**, 97370I (2016).

41. L. Bistričić et al., "Vibrational spectroscopic study of poly(dimethylsiloxane)-ZnO nanocomposites," *Vib. Spectrosc.* **68**, 1–10 (2013).
42. L. Jayes et al., "Vibrational spectroscopic analysis of silicones: a Fourier transform-Raman and inelastic neutron scattering investigation," *Anal. Chem.* **75**, 742–746 (2003).
43. L. A. Leites et al., "Vibrational and electronic spectra and the structure of crystalline poly(dimethylsi1ane)," *Macromolecules* **25**, 2991–2993 (1992).
44. R. P. S. De Campos et al., "Raman imaging spectroscopic characterization of modified poly(dimethylsiloxane) for micro total analysis systems applications," *Spectrochim. Acta Part A Mol. Biomol. Spectrosc.* **100**, 67–71 (2013).
45. M. J. Shenton, H. Herman, and G. C. Stevens, "Using spectroscopy with chemometrics to measure polymer molar mass," *Polym. Int.* **49**, 1007–1013 (2000).
46. N. E. Mircescu et al., "FTIR, FT-Raman, SERS and DFT study on melamine," *Vib. Spectrosc.* **62**, 165–171 (2012).
47. X. Chen et al., "Interaction of melamine molecules with silver nanoparticles explored by surface-enhanced Raman scattering and density functional theory calculations," *Appl. Spectrosc.* **67**, 491–497 (2013).
48. K. S. Dogbevi et al., "Self-driven microfluidic channels with controlled blood flow using an amphiphilic silicone," *ACS Appl. Polym. Mater.* **2**, 1731–1738 (2020).
49. T. Yasui et al., "DNA manipulation and separation in sublithographic-scale nanowire array," *ACS Nano* **7**, 3029–3035 (2013).

Andrew L. Cook received his BA and MA degrees in physics from the University of North Texas in 2013 and Fisk University in 2015, respectively. He earned his PhD in biomedical engineering from Vanderbilt University in 2021. He received a National Science Foundation Graduate Research Fellowship in 2015.

Todd D. Giorgio is a professor of biomedical engineering and chemical and biomolecular engineering at Vanderbilt University. He received his BS degree and PhD in chemical engineering from Lehigh University in 1982 and Rice University in 1987, respectively. He is a fellow of the Biomedical Engineering Society and the American Institute for Medical and Biological Engineering. His research interests include the solution of problems in medicine and biology using advanced functional materials.